IOP Publishing Journal of Micromechanics and Microengineering
J. Micromech. Microeng. **24** (2014) 035001 (14pp) doi:10.1088/0960-1317/24/3/035001

# Electrostatic vibration energy harvester with combined effect of electrical nonlinearities and mechanical impact

**P Basset**[1,4], **D Galayko**[2], **F Cottone**[1], **R Guillemet**[1], **E Blokhina**[3], **F Marty**[1] **and T Bourouina**[1]

[1] Université Paris-Est, ESYCOM, ESIEE Paris, France
[2] Sorbonne Universités, UPMC Univ. Paris 06, UMR 7606, LIP6, Paris, France
[3] School of Electrical, Electronic and Communications Engineering, University College Dublin, Ireland

E-mail: p.basset@esiee.fr

Received 23 July 2013, revised 20 December 2013
Accepted for publication 20 December 2013
Published 4 February 2014

**Abstract**

This paper presents an advanced study including the design, characterization and theoretical analysis of a capacitive vibration energy harvester. Although based on a resonant electromechanical device, it is intended for operation in a wide frequency band due to the combination of stop-end effects and a strong biasing electrical field. The electrostatic transducer has an interdigited comb geometry with in-plane motion, and is obtained through a simple batch process using two masks. A continuous conditioning circuit is used for the characterization of the transducer. A nonlinear model of the coupled system 'transduce-conditioning circuit' is presented and analyzed employing two different semi-analytical techniques together with precise numerical modelling. Experimental results are in good agreement with results obtained from numerical modelling. With the 1 $g$ amplitude of harmonic external acceleration at atmospheric pressure, the system transducer-conditioning circuit has a half-power bandwidth of more than 30% and converts more than 2 $\mu$W of the power of input mechanical vibrations over the range of 140 and 160 Hz. The harvester has also been characterized under stochastic noise-like input vibrations.

Keywords: vibration energy harvesting, electrostatic transduction, MEMS, mechanical impedance, VEH, e-VEH, eVEH

(Some figures may appear in colour only in the online journal)

## 1. Introduction

Vibration energy harvesters (VEHs) catch mechanical energy trough a spring–mass system and then convert the largest possible fraction of this energy into electrical power. To this end, electromagnetic, piezoelectric or electrostatic transduction can be used, and sometimes a combination of these. VEHs with electrostatic transduction (e-VEHs) display interesting features that can make a difference with the other transduction mechanisms. They are particularly suitable for fabrication using silicon-based microelectromechanical systems (MEMS) technologies through a full batch fabrication process [1–3]. Moreover, bulk crystalline silicon displays repeatable elastic properties even under strong deformations [4]. It can be used for the fabrication of nonlinear springs for wideband VEHs. The main drawback of e-VEHs is that unlike electromagnetic and piezoelectric VEHs they need to be pre-charged in order to initiate the conversion process. Therefore, in order to obtain a totally battery-free system, an electret or a piezoelectric layer needs to be added [5, 6].

One of the main issues when designing a VEH is to take into account a possible variability of the power spectral density in time and frequency. However, many VEHs are based on linear spring–mass systems and are optimized to

[4] Author to whom any correspondence should be addressed.

 

work at specific frequencies. In such structures, power is maximized only near the resonance frequency while vast majority of applications require a wideband conversion of vibration energy. The self-tuning of the operation frequency has been proposed in [7–9]. These solutions are quite efficient but require additional power for an active conditioning circuit (CC). Oscillator arrays with different resonance frequencies can also be used to obtain an overall response covering a larger frequency interval. However, this will drastically decrease the power density of a harvester [10–12]. Energy harvesting employing multi-mass oscillators has also been investigated in [13]. There is another approach that allows one to extend the frequency bandwidth of MEMS-based resonators; it consists in adding nonlinearities into their structure. Nonlinearities can be of different origins: mechanical spring softening/hardening at large oscillation amplitudes [3, 15–18], multistable potential fields [14, 19–23], electrostatic nonlinearities [24] or nonlinearities due to impact [25]. All these techniques are particularly efficient for harvesting energy from stochastic vibrations.

In 2006 we presented the first MEMS e-VEH based on the in-plane overlap-plate geometry [1, 26]. This previous design, in which silicon has been partially etched between the electrodes to reduce the parasitic capacitance, is now commonly used for e-VEH employing an electret layer. This paper presents a new silicon-based e-VEH whose variable capacitor is made of in-plane gap-closing (IPGC) interdigited combs. The IPGC architecture was initially proposed by Roundy [27], but we present here the first device able to harvest a significant amount of power in realistic conditions, i.e. moderate vibration frequency, level of acceleration and bias voltage. In addition, due to the combination of nonlinearities induced by mechanical stoppers and by the high electromechanical coupling arising from an applied bias voltage required for electrostatic transduction, energy harvesting from wideband vibration is obtained. A large half-power bandwidth of 30% has been measured, with a roughly constant converted power of about 2 $\mu$W cm$^{-2}$ below 200 Hz, all this for moderate bias voltage of 30 V and acceleration of 1 $g$.

The paper is organized as follows. Section 2 presents the results of the characterization of the capacitive transducer. Section 3 discusses the analysis of the coupled system 'transducer-CC/mechanical resonator', and section 4 presents the measurements of the electrical power converted by the system from the mechanical domain.

## 2. Description of the MEMS variable capacitor

The studied e-VEH is a conventional silicon spring–mass system with one degree of freedom [28, 29]. A movable mass is attached to a rigid frame by four linear serpentine springs. The electrostatic transducer is made of a gap-closing interdigited comb. Mechanical stoppers between the mass and the frame prevent the system from short circuits between fixed and movable comb fingers. The fabrication process is presented in figure 1. It is a full batch process that requires

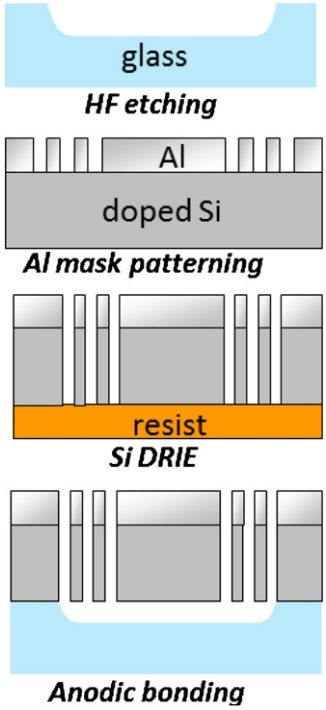


**Figure 1.** Main process steps.

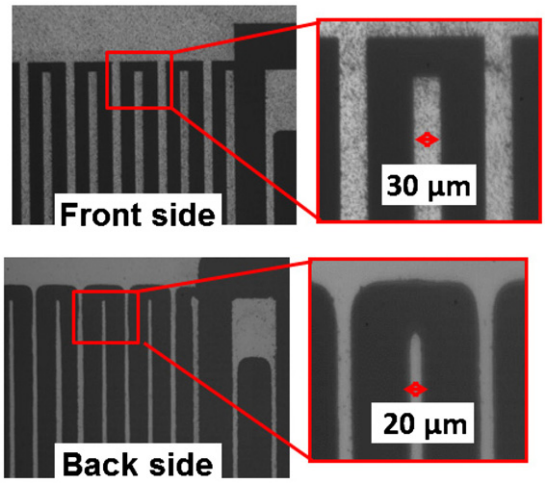


**Figure 2.** Front side and back side scanning electron microscope (SEM) views of the silicon substrate after the DRIE. A lateral etch of 0.8% is observed, leading to a trapezoidal shape of silicon beams.

only two lithography masks. An aluminum layer is sputtered on a silicon wafer and then patterned by photolithography. It is used as a hard mask to etch the movable part by deep reactive ion etching (DRIE)–Bosh process in a 380 $\mu$m-thick doped silicon wafer. Silicon etching is performed with a small slope, resulting in a trapezoidal cross section of the comb fingers and of the beam springs as shown in figure 2 [29]. After DRIE, the silicon wafer is anodically bonded onto a glass wafer that is used only as a handle wafer. Previously, the glass wafer has been etched by liquid hydrofluoric acid below the mobile part in order to allow the transducer to move. After dicing, each e-VEH is glued onto a printed circuit board that is attached to a vibrating shaker.

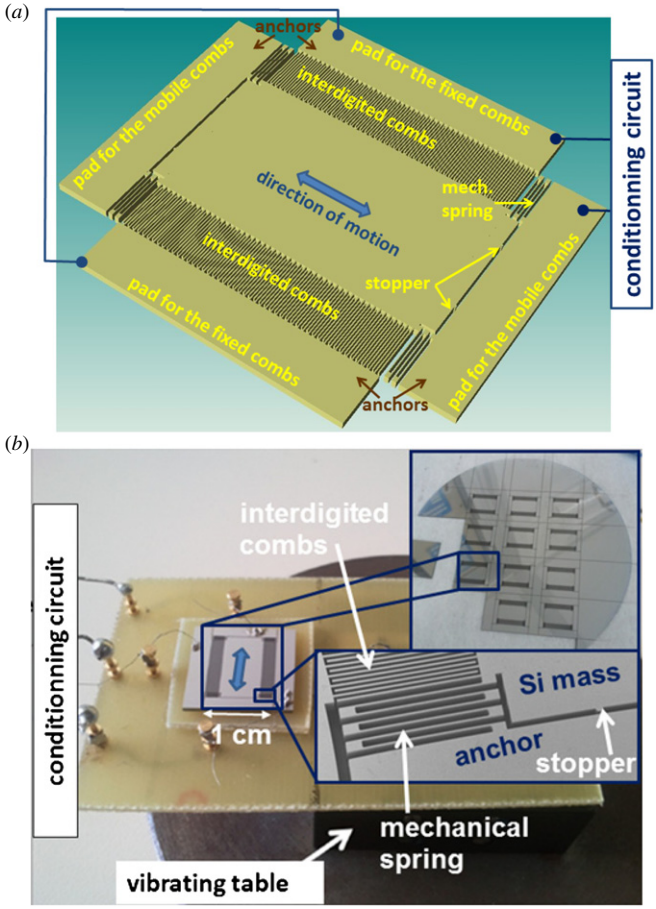


**Figure 3.** Pictures of the transducer. (*a*) 3D view from coventoreware, (*b*) photos with a SEM close-up view.

**Table 1.** Parameters of the tested e-VEH.

| Parameters | Value/Unit |
|---|---|
| Proof mass ($m$) | 66 mg |
| Elastic spring stiffness ($k_m$) | 68 N m$^{-1}$ |
| Mechanical resonance ($f_0$) | 162 Hz |
| Active area (mass + springs) | 1.1 mm$^2$ |
| Initial gap between fingers ($d_0$) | 43.5 $\mu$m |
| Stopper location ($X_{\text{lim}}$) | 36 $\mu$m |
| Load resistance ($R_L$) | 5.4 MΩ |
| Device thickness ($h_f$) | 380 $\mu$m |
| Fingers length ($l_f$) | 1.97 mm |
| Fingers width ($w_f$) | 30 $\mu$m |
| Fingers number ($N_f$) | 142 |
| Aspect ratio of sidewalls ($\alpha$) | 0.013 |

The design of the e-VEH is represented in figure 3(*a*). Its main parameters are summarized in table 1 and some of them are reported in figure 4 that shows a close-up schematic view of the interdigited combs. The variable capacitance is obtained by varying the gap between the movable and the fixed combs. The movable comb is made of 142 fingers that are 2 mm long with 1.97 mm overlap between the fixed and mobile fingers. The designed transducer gap (at the mask level) is 40.5 $\mu$m when no external acceleration is applied. Mechanical stoppers are placed to contact the movable mass after its displacement reaches 36 $\mu$m. The mobile mass is estimated to be equal to

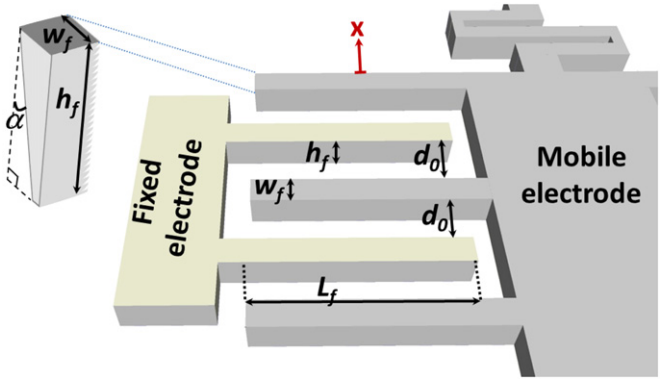


**Figure 4.** Schematic of the transducer geometry.

66 × $10^{-6}$ kg, and the total area and volume of the active parts (i.e. the area of the mass, springs and the comb fingers) are 1.1 cm$^2$ and 0.042 cm$^3$ respectively. Pictures of the device are shown in figure 3(*b*).

At this stage, it is possible to estimate the maximum power of vibrations that can be converted by this resonator independently of the electromechanical transduction mechanism. This fundamental limit on power in the case of a harmonic excitation is given by the formula [30, 31]:

$$P_{\max} = \tfrac{1}{2} A_{\text{ext}} \omega_m X_{\text{lim}} m \tag{1}$$

where $\omega_m$ is the frequency of vibration (rad s$^{-1}$), $X_{\text{lim}}$ is the maximum amplitude allowed for the mobile mass and defined, in our case, by the location of the stoppers (36 $\mu$m here), $m$ is the mobile mass and $A_{\text{ext}}$ is the acceleration amplitude of external vibrations. Taking $\omega_m = 2\pi \times 150$ rad s$^{-1}$, and $A_{\text{ext}} = 1\ g$ (the limit used in this study), one obtains 11 $\mu$W. This is the absolute limit achievable with the use of a harmonic lossless resonator having an ideal electromechanical transducer. It should be emphasized that equation (1) does not define the input power of the system. This formula only predicts the maximum power that can be transferred into the resonator from the external vibrating frame. Note that if the mechanical impedance does not match optimally, the injected power will be below this value. We also note that the injected power is 'split' into two parts: mechanical dissipation on the resonator (squeeze film damping, thermoelastic losses, etc) and mechanical power converted into electricity.

### 2.1. Dynamic capacitance measurement

Assuming negligible fringe fields and a constant slope due to the DRIE undercut, a first approximation for the capacitance of the transducer can be obtained by the integration of the expression for the capacitance of a symmetric parallel-plate capacitor whose gap is non-constant over one dimension [24]:

$$C(x) = N_f \left( \int_0^{h_f} \frac{\varepsilon l_f \mathrm{d}h}{d(h) - x} + \int_0^{h_f} \frac{\varepsilon l_f \mathrm{d}h}{d(h) + x} \right) = \frac{\varepsilon N_f l_f}{2\alpha} \ln \left[ \frac{(d_0 + 2h_f\alpha)^2 - x^2}{d_0^2 - x^2} \right] \tag{2}$$

where the sum in the parentheses is the capacitance between one movable comb finger and its two adjacent fixed comb

fingers, $N_f$ is the total number of movable fingers, $\varepsilon$ is the dielectric permittivity of air, $h_f$ is the height of the silicon substrate, $l_f$ is the length of the overlapping part of the comb fingers, $d_0$ is the gap between the fixed and movable fingers measured in the non-deformed device at the top of the comb, $\alpha$ is the ratio of the silicon undercut by DRIE. $x$ is the instantaneous displacement of the mobile electrode (with regard to the non-deformed device shape). $d(h) = d_0+2h\alpha$ is the gap between the movable finger and fixed fingers for an non-deformed structure: because of the undercut, it is a function of the coordinate $h$ defined in the direction orthogonal to the substrate plane. With a minimum gap on top of 4.5 $\mu$m corresponding to the stopper location, the theoretical nominal maximum and minimum values of $C_{\text{var}}$ are 121 pF and 41 pF. If the electrode edges were parallel with the nominal gap $d_0$, the maximum and minimum capacitances would be 221 pF and 46 pF respectively.

The goal of the experiment is to measure the evolution of the transducer capacitance over time when the device is subjected to external vibrations. The extreme values of the transducer capacitance $C_{\max}$ and $C_{\min}$ are of particular interest for electromechanical energy conversion [1]. In the considered device, the capacitance is minimal for the non-deformed device (given that there is no misalignment of the interdigited comb fingers). The measurement is carried out by dynamical detection of the phase shift in a series $RC_{\text{var}}$ circuit to which a 200 kHz/1 V peak-to-peak ac signal is applied. The capacitance is calculated as [1]:

$$C_{\text{var}} = \frac{1}{\tan(\theta)R\omega}, \tag{3}$$

where $\omega$ is the angular frequency of the source signal, $\theta$ is the phase shift between the voltage across the capacitor and the voltage generated by the source. $R$ and $\omega$ must be chosen to maximize the accuracy of the $C_{\text{var}}$ measurement, i.e. with a phase shift around $\pi/4$. The relative error of $C_{\text{var}}$ is given by [1]:

$$\frac{\Delta C_{\text{var}}}{C_{\text{var\_}m}} = -2\frac{T_s\omega}{\sin\left[2a\tan\left(\frac{1}{\omega RC_{\text{var\_}m}}\right)\right]} \tag{4}$$

where $T_s$ is the sampling period of the oscilloscope and $C_{\text{var\_}m}$ is the mean value of $C_{\text{var}}$. According to the setup parameters ($T_s =$ 10 ns, $R = 5.6$ kΩ), the mean value of the relative error of $C_{\text{var}}$ is 7%.

The capacitance variation measured at the external acceleration amplitudes of 0.25 $g_{\text{peak}}$ (at 160 Hz) and 1 $g_{\text{peak}}$ (at 150 Hz) is shown in figure 5. For the lower acceleration, the device has been excited close to its natural resonance frequency, which is found to be 162 Hz. At 1 $g$, we measured the capacitance in the middle of the band of interest as we will see in the last section. At 0.25 $g_{\text{peak}}$, using a microscope, we can optically validate that the stoppers do not reach the rigid frame. The ratio $C_{\max}/C_{\min}$∼60 pF/50 pF. At 1 $g_{\text{peak}}$, while the mobile mass strongly hits the frame (it can also be seen under the microscope), the ratio increases to ∼98 pF/50 pF. These given $C_{\max}$ and $C_{\min}$ values include the parasitic capacitance of the packaging and the measurement set-up ($C_p = 10$ pF).

Since the stoppers hit the frame at high acceleration, the exact amplitude of the mobile mass displacement is known.

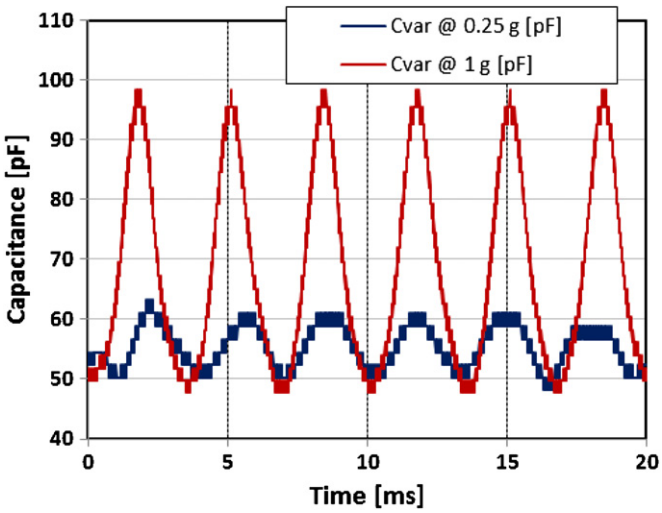


**Figure 5.** Capacitance variation with time of the transducer for an external acceleration of 0.25 $g_{\text{peak}}$ (at 160 Hz) and 1 $g_{\text{peak}}$ (at 150 Hz).

Thus, the measured value can be compared with theoretical given by equation (2). The obtained net values of the transducer capacitance (88 pF/40 pF) are less than those predicted by the design (121 pF/41 pF). The error is particularly large for $C_{\max}$. This is explained by the strong sensitivity of the transducer capacitance with respect to $x$ when $x$ is close to $d_0$. The observed discrepancy with the theory for $C_{\max}$ values suggests that one of the geometric parameters is not achieved fairly during the device manufacturing process. For example, if the initial gap $d_0$ is 3 $\mu$m larger than that was designed (43.5 $\mu$m instead of 40.5 $\mu$m), the theoretical values given by equation (2) are 90.1 and 39 pF ($C_p$ not included), which is very close to the values obtained by the measurement. It corresponds to an additional undercut of 1.5 $\mu$m at the DRIE mask level, and is a very plausible hypothesis. We keep this corrected value of $d_0$ for the simulation presented in the next section.

The presented measurement of the transducer capacitance was made using low voltage electronics. However, the experiments involving electromechanical conversion require high voltage (HV) electronics. HV electronic equipment introduces a higher input parasitic capacitance. We estimate $C_p$ in these HV experiments about 20 pF: this value is used in all simulations we present in the next sections.

## 3. Continuous-mode conditioning circuit

The role of a CC is to implement cyclic charging and discharging of the capacitive transducer $C_{\text{var}}$ as required for electromechanical conversion. In this work, the e-VEH has been evaluated with a continuous mode CC. It consists of a constant voltage source $U_0$ permanently connected to one terminal of $C_{\text{var}}$ while the other terminal is connected to a resistive load [32] (cf inset in figure 10). In practical harvesters, the voltage source is provided by a large pre-charged reservoir capacitor (few microfarads), whose voltage remains constant during an exchange of electrical charges with a small transducer capacitance. Since the charge–discharge

process is cyclic and the overall charge is conserved in the circuit, on average, no energy is consumed from the reservoir. For practical reasons, our experiments were done with a voltage source: this substitution has no impact on the system behavior. Due to the dc biasing of the $R_{\text{load}}C_{\text{var}}$ circuit, the variation of the transducer capacitance induces an ac charge flowing through the load that dissipates the energy converted from the mechanical domain. Depending on an application, the resistor may be replaced by an electronic circuit that will transform the harvested electrical energy into a form appropriate for a load supply (e.g., as in [32–34]).

### 3.1. Behavior of the conditioning circuit

Below we give a discussion that provides an understanding of the operation of this CC depending on the value of the load resistance.

*3.1.1. $R_{load} = 0$.* This is an extreme case that corresponds to an electrostatic transducer biased by a constant voltage. Such a system has been thoroughly studied in the literature. The transducer is equivalent to a nonlinear spring whose force-displacement characteristic is given by the following equation:

$$F_t = \frac{1}{2}U_0^2\frac{\partial C_{\text{var}}(x)}{\partial x}. \tag{5}$$

This force is added to the mechanical spring force. For a gap-closing transducer, $F_t$ increases with the displacement $x$ faster than linearly. $F_t$ is attractive and acts in opposition to the restoring mechanical spring force. Consequently, $F_t$ leads to an effective softening of the resonator spring and therefore to a negative shift in the resonance frequency. The softening effect depends on the vibration amplitude and is stronger if the vibration amplitude increases.

When the capacitance changes from $C_{\min}$ to $C_{\max}$, there is an average current flowing though the transducer at each half of the oscillation cycle. It is equal to:

$$I_{\text{av\_max}} = \frac{2U_0(C_{\max} - C_{\min})}{T_e} \tag{6}$$

where $T_e$ is the period of the transducer capacitance variation (note that it can be different from the period of external vibrations). $I_{\text{av\_max}}$ is the upper limit of the average transducer current which can only be reached when $R_{\text{load}} = 0$. However, the average converted power is zero for $R_{\text{load}} = 0$ since there is no voltage variation across the capacitor.

*3.1.2. $R_{load}$ is small such that $I_{av\_max}R_{load} \ll U_0$.* In the case when $R_{\text{load}}$ is such that $I_{\text{av\_max}}R_{\text{load}} \ll U_0$, the voltage drop across the resistor is negligible compared to $U_0$. The voltage across the transducer terminals can be considered equal to $U_0$. The power dissipated by the resistor is proportional to the resistance value. From the mechanical point of view, the context is exactly as in the previous case. However, since there is a real power dissipated by the resistor, the converted power is non-zero, although small. This electromechanical conversion has a small impact on the mechanical dynamics of the system.

*3.1.3. $R_{load}$ is large such that $I_{av\_max}R_{load}$ is of the same order of magnitude as $U_0$.* This is the case of interest for energy harvesters: a non-negligible amount of mechanical energy is converted into the electrical domain and is dissipated through $R_{\text{load}}$. As we shall see in the next section, the equation that describes the system cannot be solved analytically for this case. The real part of the transducer mechanical impedance increases, and so does the converted power. In this case, the presence of the resistor cannot be neglected in the analysis of the mechanical behavior of the system.

*3.1.4. $R_{load}$ increased toward very large values.* This is another extreme case. The current through the resistor decreases, and the charge flow between $C_{\text{var}}$ and $U_0$ is impeded. If $R_{\text{load}}$ is extremely large, there is no current, the converted power is zero and the transducer operates in constant charge mode. In this case, the only influence of the CC on the transducer is a frequency shift in the mechanical resonance due to a phenomenon known as nonlinear electrostatic spring. The electrostatic force is now given by:

$$F_t(x) = \frac{1}{2}\frac{Q_0^2}{C_{\text{var}}^2(x)}\frac{\partial C_{\text{var}}(x)}{\partial x}. \tag{7}$$

Here $Q_0$ is the bias charge of the capacitor. In this context, $F_t$ is defined from the transient process described by the model presented in the next section.

We note that the electrostatic force given by equations (5) and (7) depends on the geometry of a transducer. For example, for a gap-closing transducer with parallel walls, equation (5) gives a non-zero function while equation (7) gives zero. Since the studied device has a transducer with a geometry resembling an ideal gap-closing transducer, we expect similar, although not exactly equivalent, behavior. This is confirmed by numerical simulations presented in the next section.

### 3.2. Modeling of the system

Similarly to all CCs for e-VEHs [33–35], the continuous mode CC shown in figure 10 is nonlinear. The corresponding ordinary differential equation (ODE) cannot be solved in closed form and can only be studied using an ODE solver (Matlab, Scilab, VHDL-AMS, VerlogA or other). The mathematical model we used for this study is suitable for VHDL-AMS/Eldo based simulation [36]. The system dynamics are described in a three-dimensional state space where the state variables are the instantaneous transducer charge $q$, the displacement $x$ and the velocity $v$. The differential equations are derived from the mesh law describing the voltages in a single mesh of the CC and from the Newton law written for the resonator, when no impact occurs between the mobile mass and the stoppers:

$$\begin{cases} \dot{q} = \left(U_0 - \frac{q}{C_{\text{var}}(x)}\right) \Big/ R_{\text{load}} \\ \dot{v} = A_{\text{ext}}(t) - \frac{k}{m}x - \frac{\mu}{m}v + \frac{1}{m}F_t(x, v) \\ \dot{x} = v \end{cases} \tag{8}$$

$C_{\text{var}}(x)$ given by equation (2), $A_{\text{ext}}(t)$ is the time evolution of the acceleration of external vibrations, $m$, $k$ and $\mu$ are the resonator lumped mass, stiffness and damping respectively. $F_t$

is the force generated by the transducer on the mobile mass, which can, in general, depend on the displacement, the velocity and the transducer charge. The damping factor $\mu$ is related to the intrinsic quality factor of the resonator connected to a zero-biased transducer:

$$\mu = \frac{\sqrt{\mathrm{km}}}{Q} \tag{9}$$

where $Q$ is the quality factor of the resonator. It should be noted that our structure is tested under atmospheric pressure, and the main origin of the damping is squeeze film damping of the air layer between the transducer electrodes. In this model, damping is supposed to be linear, but in reality it depends on the amplitude of vibrations: the higher is the amplitude, the stronger is the damping since the smallest is the gap between the electrodes at the maximum displacement. In the analysis presented in this section, we will give the value of an 'effective' quality factor for each simulation of model equation (8) by fitting the model with the measurements. We have estimated that $Q \approx 8.5$ for small vibration amplitudes. For high vibration amplitudes, the squeeze film damping is strong and the system is nonlinear: hence, the quality factor notion is not applicable to the system. However, we estimate the effective quality factor of an 'equivalent' linear resonator to be $Q \approx 4.5$: it provides a correct prediction of the resonator vibration amplitude for strong input acceleration, as it will be shown in figure 14.

In the absence of contact with the stoppers, the transducer force $F_t$ depends only on $x$ and on the transducer charge $q$:

$$F_t(x) = \frac{1}{2}\frac{q^2}{C_{\mathrm{var}}^2(x)}\frac{\partial C_{\mathrm{var}}(x)}{\partial x}. \tag{10}$$

However, because of electrostatic instability, it is difficult to use this model 'as is': during the transient process, an amplitude overshoot may induce the pull-in phenomenon forcing the simulation to crash. Hence, the stopper effect should be modeled at least to limit the displacement of the mobile mass and, ideally, to model the dynamics of the impact process correctly. In our stimulations, we have used the following model for the rebound force applied by each stopper to the movable mass:

$$F_{\mathrm{stop}}(x, v) = \begin{cases} -k_{\mathrm{stop}}(d_0 - d_{\mathrm{stop}} - x)\mathrm{sign}(x) - \mu_{\mathrm{stop}}V, & \mathrm{abs}(x) > d_0 - d_{\mathrm{stop}} \\ 0 & \text{otherwise} \end{cases} \tag{11}$$

where $d_{\mathrm{stop}}$ is the minimal gap allowed between the transducer electrodes by the stoppers, $\mu_{\mathrm{stop}}$ and $k_{\mathrm{stop}}$ are the damping and stiffness of the stoppers. The $d_{\mathrm{stop}}$ value is defined by the structure design and is known a priori. Several studies have addressed the estimation of $\mu_{\mathrm{stop}}$ and $k_{\mathrm{stop}}$, and the fitting of approximated analytical models appears to be the mainstream technique [25]. We used 1 Ns m$^{-1}$ for $\mu_{\mathrm{stop}}$ and $10^4$ N m$^{-1}$ for $k_{\mathrm{stop}}$.

### 3.3. Prediction of the optimal load and the harvested power

The power dissipated by a resistive load can be calculated as:

$$P_{\mathrm{Rload}} = \frac{1}{t_2 - t_1}\int_{t_1}^{t_2}\frac{U_{\mathrm{load}}^2}{R_{\mathrm{load}}}\mathrm{d}t \tag{12}$$

where $U_{\mathrm{load}}$ is the voltage on $R_{\mathrm{load}}$ related to the charge $q$ in equation (8) as $U_{\mathrm{load}} = \dot{q}R_{\mathrm{load}}$. It is not possible to calculate the integral in equation (8) in closed form. However, this expression can directly be used for an experimental measurement of the converted power. The output voltage $U_{\mathrm{load}}$ is, in general case, alternating and non-harmonic. Two techniques that we discuss below can provide an insight into the link between the system parameters and the converted power: mechanical impedance approach and charge–voltage diagrams.

*3.3.1. The mechanical impedance approach.* The analysis based on the mechanical impedance describes the dynamic behavior of a mobile mass in the mechanical domain by analyzing the mechanical contribution of a transducer coupled with a CC accounting for nonlinear features of these components [37]. The mechanical impedance of an electromechanical transducer associated with a given CC can be defined in the context of energy conversion systems. If the mobile terminal of the transducer displays sinusoidal motion with the amplitude $X$, and the transducer generates a periodic electrostatic force with the same frequency but not obviously sinusoidal (the transducer is nonlinear in general case), the mechanical impedance of the transducer $\Psi_t$ is given by [37]:

$$\psi_t = -\frac{\dot{F}_t^{\omega}}{\dot{V}} = -\frac{\dot{F}_t^{\omega}}{j\omega_m\dot{X}} \tag{13}$$

where $\dot{F}_t^{\omega}$ is the complex amplitude of the first harmonic of the transducer force at a frequency $\omega_m$ of the mobile terminal displacement and the dotted $X$ and $V$ are the complex amplitudes of the displacement and the velocity of the mobile terminal respectively. It is very important to remember that, since the system is nonlinear, $\Psi_t$ depends on the amplitude $X$. When the transducer is associated with a mechanical system (a resonator), the actual complex amplitude of the mobile mass vibration is given by the second Newtonian law expressed by the following nonlinear algebraic equation [37]:

$$\dot{F}_{\mathrm{ext}} = -\left[\psi_t(X) + \psi_r\right] j\omega_m\dot{X} \tag{14}$$

where $\dot{F}_{\mathrm{ext}}$ is the complex amplitude of the inertial force applied to the mobile mass because of external vibrations [38] and $\Psi_r$ is the mechanical impedance of the resonator.

If the amplitude of the resonator vibrations is known, the converted power is immediately calculated through the transducer mechanical impedance [37]:

$$P_{\mathrm{converted}} = \tfrac{1}{2}(\omega_m X)^2\,\mathrm{Re}\,(\psi_t) \tag{15}$$

where $\omega_m$ is the angular frequency of mechanical vibrations, $\Psi_t$ is the transducer impedance and $X$ is the amplitude of the mobile mass displacement. Note that equations (12) and (15), which allow one to calculate the converted power in the electrical and mechanical domains respectively, provide identical value of converted power.

Figure 6 shows the charts of transducer mechanical impedance calculated for three values of the bias voltage $U_0$ for the maximum amplitude allowed by the stoppers (36 $\mu$m) when the resistance of the load changes from 100 k$\Omega$ to 500 M$\Omega$. Several conclusions can be made based on the analysis of the mechanical impedance:

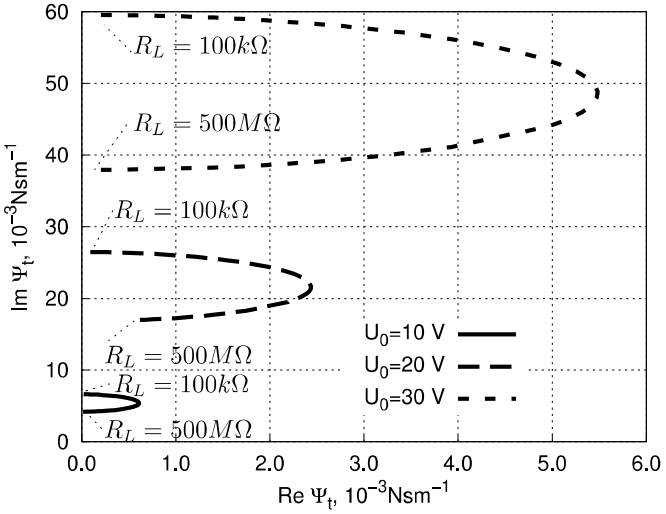


**Figure 6.** Mechanical impedance chart of the transducer-conditioning circuit block versus load resistance. $X = 36$ $\mu$m, $R = 100$ k$\Omega$, . . . ,500 M$\Omega$.

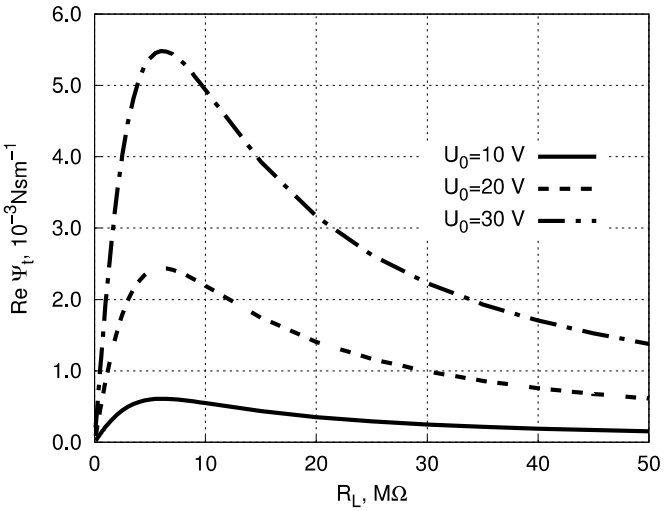


**Figure 7.** Real part of impedance of the transducer-conditioning circuit block versus load resistance. $X = 36$ $\mu$m, $f_m = 150$ Hz, $R = 100$ k$\Omega$, . . . ,50 M$\Omega$. The resistance value corresponding to the maximal power is 6 M$\Omega$—the same for the three plots.

- The value of the impedance is linearly scaled as the square of $U_0$.
- As is expected, the imaginary part of the impedance responsible for the electrostatic spring softening phenomenon is positive. It is large for low values of the load resistance and decreases at high values of the load resistance.
- As the load resistance increases from low values to very large values, the real part of the mechanical impedance increases, reaches a peak value and then decreases. There is an evident correspondence with the four typical cases of $R_{\text{load}}$ considered previously in this section (cf also equation (15) giving the converted power).
- Since the impedance is calculated for a fixed amplitude of the mobile terminal, the converted power is proportional to the real part of the transducer impedance, according to equation (15). For $U_0 = 30$ V, it corresponds to 3.2 $\mu$W.

Figure 7 shows the real part of the transducer mechanical impedance versus the load resistance. As can be seen from the figure, the optimal $R_{\text{load}}$ maximizing the converted power is the same for all voltages $U_0$ and is equal to 6 M$\Omega$.

It is important to point out that the figures showing the converted power that we present and discuss in this section are valid under assumption that the amplitude of the mobile electrode of the transducer is fixed and is known. Obviously, the power calculated using this approach could increase unlimitedly if the voltage $U_0$ increases. This contradicts to the realistic behavior of the system since the system, 'transducer-CC' is analyzed separately from the dynamics of the resonator in the mechanical domain. Such a 'separate' approach gives an insight only into the properties of the electromechanical conversion process. The actual displacement of the mobile mass and the actual converted power can only be found from equation (14) taking into account all components of the system.

*3.3.2. The charge–voltage diagram approach.* Charge–voltage diagrams ($QU$) provide a good intuitive insight into the energy conversion process achieved by a capacitive transducer [34]. Such a diagram is a trajectory of a capacitive transducer in the space spanned by the state variables 'charge $Q$' and 'voltage $U$'. If the behavior of the system is cyclic, its $QU$ diagram is also a cycle whose area is equal to the energy converted during one cycle. Figure 8 shows typical $QU$ cycles of the studied CC obtained assuming the maximum displacement of the mobile mass (36 $\mu$m). The two extreme cases ($R_{\text{load}}$ is very small or very large), the maximum power case ($R_{\text{load}} = 6$ M$\Omega$) and a non-specific case for $R_{\text{load}} = 10$ M$\Omega$ are shown in this figure. It can be seen that the cycles plotted for small and large $R_{\text{load}}$ (100 k$\Omega$ and 200 M$\Omega$) are virtually degenerated into a line, so that their area and hence the converted power is close to zero.

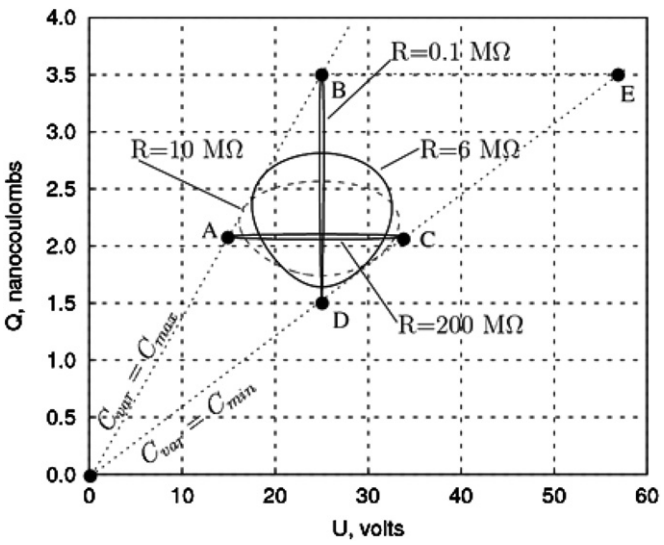


**Figure 8.** $QU$ cycles for small (0.1 M$\Omega$), optimal (6 M$\Omega$), intermediate (10 M$\Omega$) and high (200 M$\Omega$) values of $R_{\text{load}}$. $X = 36$ $\mu$m, $U_0 = 30$ $V$, $f_m = 150$ Hz. In dot lines are shown two alternatives QU cycles which can be achieved with the same bias voltage: constant charge (OBE) and constant voltage (OBD).

At this point, it is interesting to compare the operation of this CC with a CC implementing a triangular constant-charge $QU$ cycle (e.g., as in [34]). During the constant-charge cycle, the transducer is pre-charged to $U_0$ when its capacitance is maximal. Such a $QU$ cycle is also shown in the figure 8 by dashed lines forming the triangle OBE. It can easily be seen that the constant-charge triangular $QU$ cycle is much larger than the $QU$ cycle of the studied CC plotted for the optimal $R_{\text{load}}$ value. The power converted during the constant-charge $QU$ cycle is given by the formula [34]:

$$P_{\text{const}Q} = \frac{1}{2}U_0^2 C_{\max}\left(\frac{C_{\max}}{C_{\min}} - 1\right) f_e. \tag{16}$$

At the amplitude $X = 36$ $\mu$m, $C_{\max} = 110$ pF, $C_{\min} = 59$ pF including a 20 pF parasitic capacitance, $f_e$ is the frequency of the capacitance variation and is twice the frequency of the mechanical vibrations $f_m$ ($f_m = 150$ Hz for this simulation). At $U_0 = 30$ V, equation (16) gives 12.8 $\mu$W. The comparison is less disadvantageous for the studied circuit if the latter is compared to the constant-voltage triangular $QU$ cycle also given in figure 8 as the triangle OBD. In this case, the power is calculated using the formula [34]:

$$P_{\text{const}U} = \tfrac{1}{2}U_0^2 (C_{\max} - C_{\min}) f_e. \tag{17}$$

This formula predicts 6.9 $\mu$W of power.

For our circuit, the converted power calculated using the real part of the impedance equation (15) at $U_0 = 30$ V and $R_{\text{load}} = 6$ MΩ (see figure 7) yields only 3.2 $\mu$W. As a result, while the continuous mode CC is very simple to implement, its theoretical performance is weaker comparing to other circuits ensuring best power conversion scenarios. We note that the power values calculated in this section are obtained without accounting for the power available in the mechanical domain, since the mobile mass vibration amplitude was assumed of a given amplitude. Hence these values can be greater than one given by equation (1), as it is the case for the constant-charge CC.

### *3.4. Influence of nonlinear forces: resonator softening and hardening behavior*

In this section we discuss on the influence of mechanical nonlinearities on the harvester behavior. The plot in figure 9 presents the typical mechanical forces acting on the mobile mass in function of the resonator displacement. There are three main forces: the spring return force, the stopper force and the force generated by the electrostatic transducer. In figure 9, we show two kinds of forces generated by the spring: a linear restoring force (an ideal case) and a restoring force with a third-order nonlinearity (a more realistic case). At low displacement, these two curves are identical, and the third-order nonlinear force becomes greater for large displacement. This phenomenon is responsible for the resonator's spring stiffening effect well studied in theoretical mechanics (cf study of Duffing resonator in [39]). The resonator stiffening phenomena can be understood by considering that the stiffness of the resonator is the average of the slope of the spring force on the mobile mass trajectory (this is mathematically not correct but roughly provides a good intuitive understanding of the observed phenomena). It can be seen that for nonlinear spring, the average slope is larger than for a linear one. Moreover, the average slope increases with the amplitude.

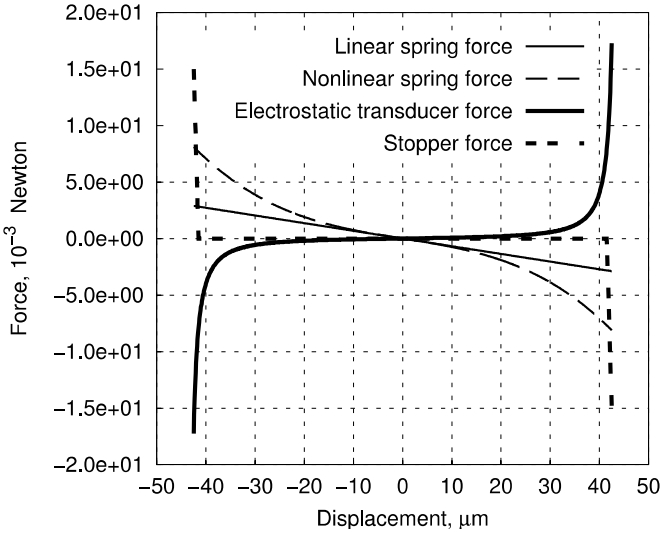


**Figure 9.** Typical sketch of different forces acting on the resonator.

The stopper stiffness is much stronger than the stiffness of the resonator spring. When the theoretical displacement amplitude of the resonator is above the stopper location, the spring restoring force is superposed with the bump stopper force [25] and the average stiffness drastically increases. Then the 'stiffening phenomenon' appears, leading to an increase of the frequency of maximum mass displacement [40], similarly to the case of the Duffing resonator.

The electrostatic force plotted in figure 9 is calculated for a transducer biased by a fixed voltage $U_0$. This is not strictly correct for our circuit, since when the resonator moves, there is a current which produces a voltage on the load resistance, and hence a variation of the voltage on the transducer. However, because of its complexity, this effect is neglected in the below explanation, providing an intuitive insight into the device physics. It can be seen that the plotted electrostatic force is positive and is growing for positive displacements: it means that this force models a negative stiffness [40]. When superposed to mechanical forces, electrostatic force contributes to a softening of the resonator.

For small displacement, the slopes of the spring and electrostatic forces are almost constant, and the negative stiffness of the transducer is added to the mechanical spring stiffness: the resonator is softened. For larger amplitude inferior to the stopper position, these two forces become progressively nonlinear and the resonator can be softened or hardened, depending on whose slope of force-displacement characteristic is the highest. This depends on the resonator/transducer geometry and on the voltage applied on the transducer. For very large amplitude, the resonator hits the stoppers and is hardened because the stoppers are much 'stiffer' than any other forces.

We can note that there is one more nonlinear force acting on the resonator: the squeeze-damping force. It contains a dissipative term (i.e., dependent on the velocity) and an elastic one (i.e., dependent on the displacement) [40, 41]. Both

terms are amplitude-dependent, and they increase nonlinearly when the resonator mobile mass comes close to the stoppers, so contributing to the spring stiffening effect. The elastic term has not been taken into account in this study, as the nonlinear amplitude dependency of the dissipating term. Instead, as mentioned previously, an effective constant quality factor (obtained by fitting the experimental curves) has been introduced in the model.

The main consequence of the softening and hardening of the resonator is a variation of the 'average' resonator stiffness, and hence of the actual resonance frequency. Since, as it is explained above, the stiffening/softening phenomena depends on the mobile masse amplitude and bias voltage, the resonator can respond by high amplitude vibrations at frequencies which are different from its natural resonance frequency. Moreover, since the resonator amplitude has an influence on the resonator resonance frequency, the whole frequency response can be very strongly impacted by the nonlinearities. As it was shown in other works, typical effects of spring stiffening due to stoppers and to high order spring nonlinearity is an increase of the resonator bandwidth [25, 42]. As shown by the experiments described in the next sections, this is also true for the designed resonator.

## 4. Measurement of converted power

The first set of measurements has been performed at atmospheric pressure and at two levels of the external harmonic acceleration amplitude $A_{ext}$, 0.25 $g_{peak}$ and 1 $g_{peak}$ respectively. It was observed that at $A_{ext} = 0.25\ g$ the mobile mass does not reach the limits defined by the stoppers: we call this regime 'non-contact mode'. At $A_{ext} = 1\ g_{peak}$, the mobile mass hits the rigid frame. The impact of the mobile mass and the stoppers has been both observed under a microscope and confirmed by the measurements. The second set of measurements presents the behavior of the system under input stochastic noise vibrations. The main goal of the experiments is to provide the relation between the converted power and the parameters of the experiment: the frequency, the initial voltage $U_0$, the load resistance and the input vibration amplitude. The output power is calculated using equation (12), and the voltage is directly measured across the load resistor employing a high input impedance voltage amplifier. Since the goal of a capacitive transducer in the context of energy harvesting is to convert maximum power, all power measurements are carried out at the frequency corresponding to the maximal power, unless otherwise mentioned.

Prior to the measurements of the converted power, the resonance frequency of the resonator as a function of the applied bias voltage was studied. Figure 10 shows the value of the external vibration frequency at which the harvested power is maximal for bias voltages varying from 0 to 40 V. As is expected, the spring softening effect typical for gap closing transducers occurs when $U_0$ increases, demonstrating the possibility to tune the harvester over a large range of frequencies, from its natural resonance $f_0$ to almost half of it. This effect comes from the shape of the relationship between the electrostatic force and the mobile electrode

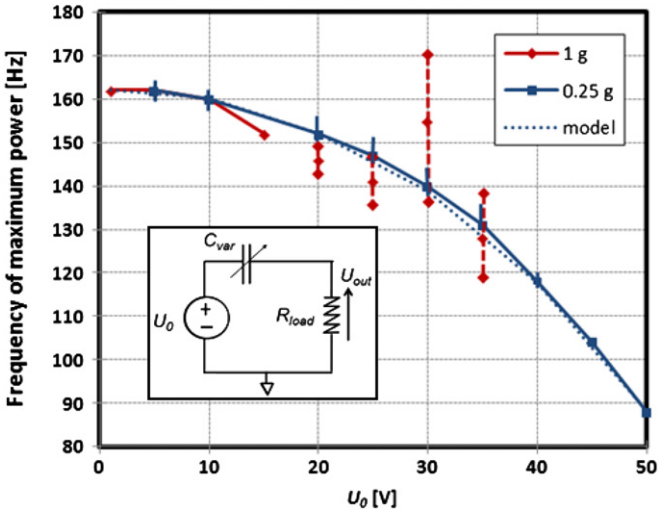


**Figure 10.** Frequencies of the maximum harvested power with respect to the bias voltage. The vertical bars represent the frequency range corresponding to more than 90% of the maximum power.

displacement which is a function of $U_0$ [40], cf the discussion above in section 3.4. The formula describing the shift of the resonance frequency associated with a parallel-plate gap-closing transducer in small-displacement mode is given by:

$$f = f_0\sqrt{1 - \frac{k_e}{k_m}} = f_0\sqrt{1 - \frac{C_0U_0^2}{k_m d_0^2}} \tag{18}$$

where $C_0$ and $d_0$ are the initial gap and capacitance and $k_m$ is the linear stiffness of the mechanical spring with $d_0 = 43.5\ \mu$m. For the acceleration amplitude of 0.25 $g_{peak}$, the observed curve can be accurately fitted using equation (18).

### *4.1. Operation without impact with stoppers (moderate vibration amplitude)*

All measurements presented in this sub-section have been carried out at the 0.25 $g$ external vibration amplitude. In this mode, the amplitude of the resonator vibrations is smaller than the transducer gap, and there is no impact with the stoppers.

For the first set of measurements, we looked for the optimal resistive load. Figure 11 shows the converted power $P_{Rload}$ versus $R_{load}$ for different applied dc voltages $U_0$. The optimum load is almost independent on $U_0$ and is around 6–7 MΩ. The experiments at $U_0 = 10$, 20, 30 and 40 V have been modeled by equation (8) with the quality factor $Q = 8.5$ (cf Section 2). The corresponding curves are also shown in figure 11. They are in very good agreement with the experiment except for the curve at $U_0 = 40$ V. In this case, the power given by the numerical simulations is overestimated by about 25%. This discrepancy can have two explanations. The first one is related to nonlinear damping of the air film in-between the transducer electrodes. Indeed, the simulations predict a slight increase of the vibration amplitude when the bias voltage increases (from 20 $\mu$m for $U_0 = 10$ V to 26 $\mu$m for $U_0 = 40$ V). As is mentioned in section 3, when the vibration amplitude of the mobile mass increases, the squeeze film damping increases. Since this phenomenon is not

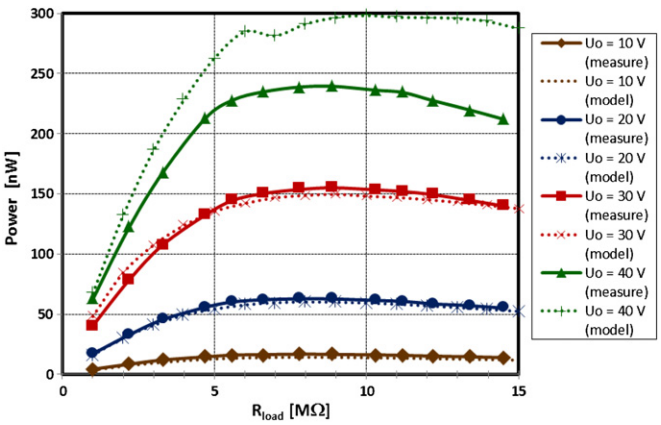


**Figure 11.** Measured and calculated (with $Q = 8.5$) harvested power with respect to the resistive load for an acceleration of 0.25 $g_{peak}$ and various bias voltages.

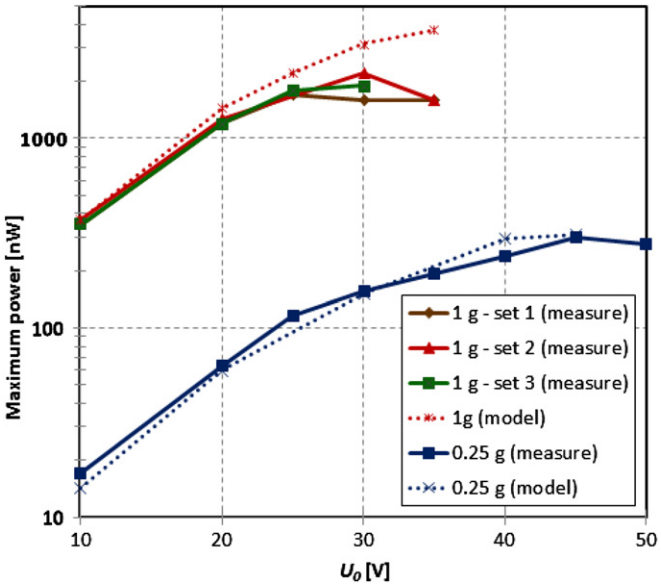


**Figure 12.** Maximum power harvested at the optimum frequency defined in figure 10 for an acceleration of 0.25 $g_{peak}$ and 1 $g_{peak}$ with respect to the bias voltage.

incorporated into equation (8) that uses a constant effective $Q$-factor instead, there is an overestimation of the vibration amplitude and, hence, of the converted power. The second explanation of the discrepancy concerns the uncertainty on the electrostatic transducer geometry used in the model. This discrepancy could be negligible for low values of $U_0$ and small mass displacements when the electrostatic force is not predominant, but it is not the case for high values of $U_0$.

Figure 12 shows the maximum harvested power at optimal $R_{load}$ versus the bias voltage. As is expected, the power increases as almost the square of $U_0$ (actually it increases as $U_0^{1.9}$). However, at large $U_0$ the power never exceeds some limit which is posed by the fundamental formula equation (1). There is a good match between the experimental figures and the values of power predicted by numeric simulations of the model equation (8).

The converted power measured during a frequency sweep is shown in figure 13. With a pre-charge $U_0$ up to 30 V, the

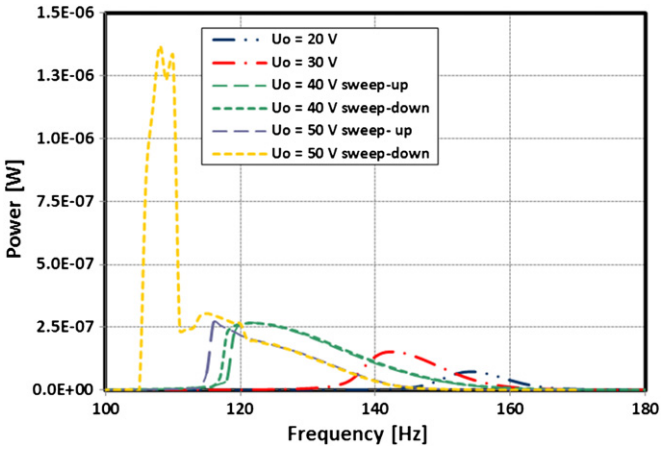


**Figure 13.** Harvested power measured for up and down frequency sweeps at 0.25 $g_{peak}$ for various bias voltages.

frequency sweep-up and sweep-down curves are identical. But beyond 30 V, a hysteresis appears due to increasing nonlinearities related to the electrostatic transducer. This is a typical behavior for a Duffing oscillator. At 50 V, irregular behavior is observed. At higher voltages electrostatic instability takes place, and the mobile electrode sticks on the stoppers.

### *4.2. Impact mode (strong vibration amplitude)*

All measurements presented in these sub-sections have been carried out at the external vibration amplitude of 1 $g$. With such an input excitation, at the resonance frequency, the zero bias voltage (i.e. only mechanical behavior is considered) and the quality factor $Q = 8.5$, the theory predicts that the mobile mass hits the stoppers. From the formula for the mobile mass displacement:

$$X = \frac{mA_{ext}}{\mu\omega_m} \tag{19}$$

one can find that $X$ is about 82 $\mu$m. Since the quality factor is expected to decrease when the amplitude increases, lower value of $Q$ should be considered for modeling this large-displacement mode. Therefore, the dynamics of the mobile mass motion may be complex, and our analytical model is not reliable anymore (in particular due to of unknown mechanical parameters of the stoppers). Moreover, when the transducer is biased, a nonlinear electrostatic force field is superposed on the mechanical force field due to the resonator spring and to the stoppers, yielding to a complex potential field [43].

Figure 14 presents the converted power versus the load resistance at different $U_0$. As is expected, the power increases with the increase of the bias voltage, although there is a limit observed at HV values, as in the similar experiment at $A_{ext} = 0.25\ g$. We assume that at this stage, the squeeze-film damping provides a dominant contribution to the dissipation of power. To take this into account, we reduced the quality factor to 4.5 in our model, and after this modification, the results of numerical simulations fit well the experimental data for low $U_0$ (figure 14). Similar discrepancies between the simulation results and the experiment as shown in figure 11 are observed for high bias voltages.

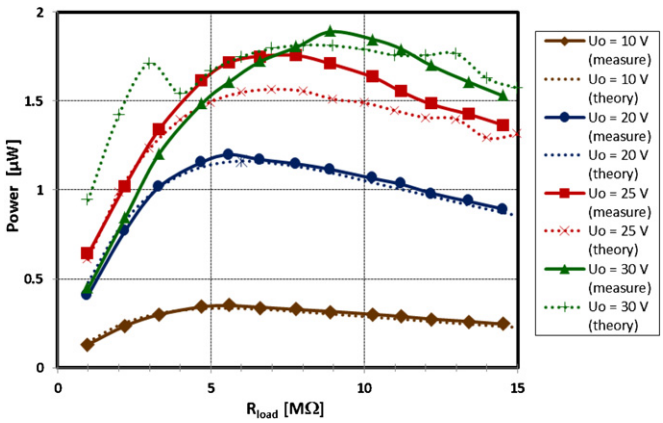


**Figure 14.** Measured and calculated (with $Q = 4.5$) harvested power with respect to the resistive load for an acceleration of 1 $g_{peak}$ and various bias voltages.

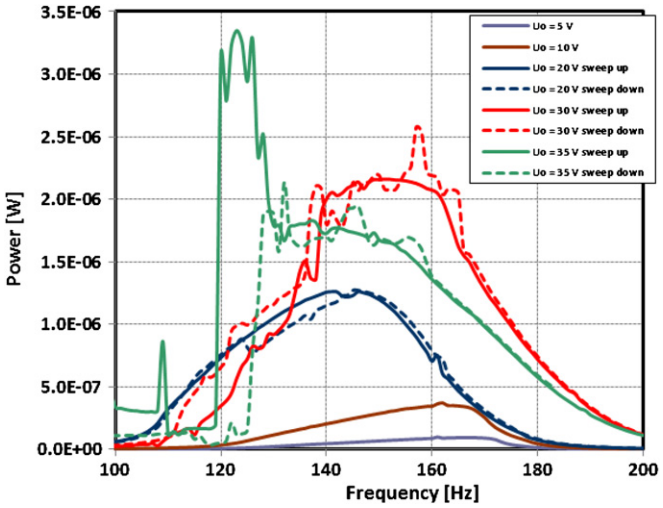


**Figure 15.** Harvested power measured for up and down frequency sweeps at 1 $g_{peak}$ for various bias voltages.

Figure 15 shows the measurement of the converted power when the frequency of external harmonic vibrations is swept up and down. For small values of $U_0$ up to 20 V, the frequency that corresponds to the maximum power decreases when $U_0$ increases. This may be explained by the spring softening effect related to the presence of a biased electrostatic transducer as is shown in figure 10 for 0.25 $g$ acceleration, whereas there is no impact with stoppers for these voltages. Almost no hysteresis is observed, meaning that the nonlinearities are not very strong: as we explained in section 3.4, for average amplitudes, the mechanical nonlinearity of the spring can compensate the nonlinearity of the electrostatic transducer. Then above 20 V, the frequency that corresponds to the maximum power increases. This, in its turn, is explained by a spring stiffening effect, arising from the impact with the stoppers and the effect of high squeeze-film damping (cf section 3.4). At 30 V of applied dc voltages, we observed a drastic increase of the bandwidth toward high frequencies. The half-power bandwidth is 30% of the central frequency, and the harvested power is above 2 $\mu$W in the band. The power has roughly identical evolution when the frequency is swept up and down, although small power spikes are observed on the sweep-down curve suggesting the beginning of irregular behavior of the mobile mass. From 35 V, the measured power curve becomes very irregular: it is difficult to interpret the dynamic of the system considering just a superposition of different factors studied above. At 50 V almost no more power is harvested due to sticking of the electrodes.

In the theory of nonlinear resonators (Duffing oscillators), the softening/stiffening effects are often accompanied with hysteresis in the frequency response. In our measurement, virtually no hysteresis was observed up to $U_0 = 30$ V. This is probably due to the presence of a strong damping component introduces by the squeeze film damping and the load resistance. More generally, as described previously, many factors impact on the system dynamic, and because of nonlinearities, it is difficult to interpret their collective contributions. In particular, two factors are difficult to model accurately: the stopper effects and the squeeze film damping at large amplitude.

The 1 $g$ curve in figure 10 shows the frequencies at which the maximum power is converted. Compared to the similar plot measured at 0.25 $g$, there is a range of frequencies (rather than a point) corresponding to the maximum power. This is because the frequency bandwidth in which the converted power is maximal is enlarged, cf the plots in figure 15. The irregular dynamics of the system at high bias voltages are confirmed by the 1 $g$ plots in figure 12. The instantaneous harvested power varies over $\pm 10\%$ for values of $U_0$ around 30 V, as demonstrated by the three sets of measurements.

The mechanical impedance method has been used to validate the measurements and to theoretically predict the converted power, rather than the model of the full system equation (8). This choice is explained by the presence of the impacts with stoppers: since there is no reliable model of stoppers, equation (8) together with equation (11) cannot accurately model the system behavior. However, since the amplitude of the mobile mass is known at the impact mode, the mechanical impedance method can immediately be applied. We note that in reality, in the impact mode, the motion of the resonator is not sinusoidal, because of the impacts with stoppers. However, since there is a periodic external force and a periodic motion of the resonator with the same frequency, a hypothesis can be made on the fact that the first harmonic dominates in the resonator motion. This allows an application of the mechanical impedance method [37, 44]. Figure 12 shows the estimated power using equation (15) and the maximum values of the real part of the mechanical impedance from figure 7. A good matching is obtained for values 10, 20 and 25 V. For 30 V the matching is less good (3.2 $\mu$W given by the theory, 1.6–2.2 $\mu$W given by the experiment). Higher values of the converted power predicted by the theory can be explained by the fact that the mechanical impedance is defined for a regular motion for a given amplitude. However, the dynamics of the mobile mass are not fully regular at 30 V, and the variable capacitor may not reach the maximum value at each cycle. As a result, equation (15) provides the upper limit of the converted power, and the difference between the measured and calculated power is not surprising.

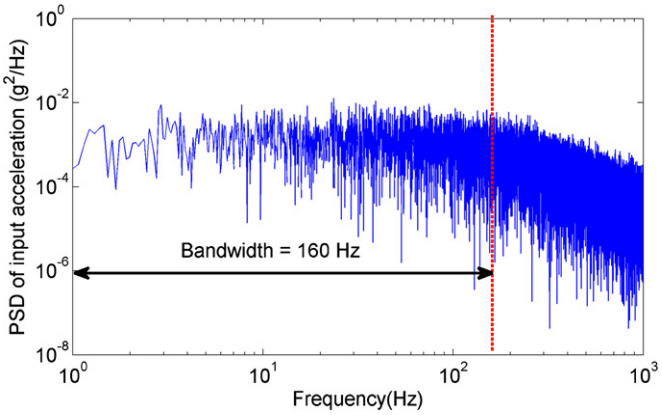


**Figure 16.** Input excitation PSD for the experiment with stochastic noise: band-limited colored noise with acceleration level of 1 $g_{rms}$ distributed over a bandwidth of 160 Hz.

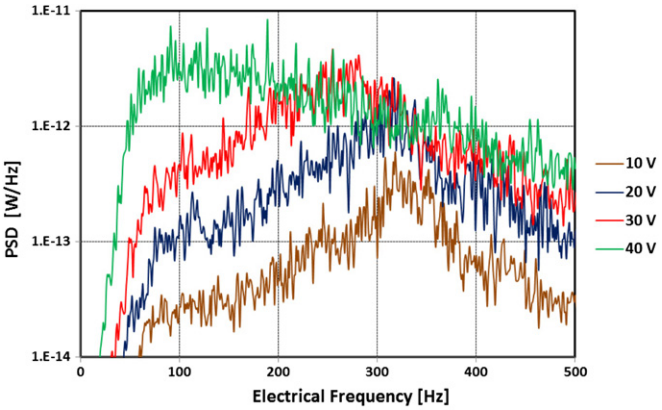


**Figure 17.** Power spectral density of the harvested power for the color noise in figure 16 for various bias voltages.

### *4.3. Stochastic excitation*

Figure 17 shows the response of the e-VEH actuated by applying exponentially correlated noise whose characteristic is shown in figure 16. The autocorrelation time of noise is 0.01 s (i.e. cut-off frequency of 160 Hz). The total acceleration level spread over this bandwidth is 1 $g_{rms}$, i.e. the mean input acceleration power spectral density (PSD) is ∼0.006 $g^2$ $Hz^{-1}$ below the cut-off frequency. At low $U_0$ (up to 20 V), the system behaves as a resonant mechanical system. This can be seen from a well-defined maximum of the converted power in the spectrum of the output electrical signal. The peak of power occurs at the frequency roughly given by equation (18) multiplied by 2. From 30 V, the bandwidth of the spectral density of the harvested PSD starts increasing. The maximum bandwidth occurs at 40 V, with the maximum harvested power for vibrations around 50 Hz (the observed spectrum peak frequency divided by 2). It can be seen that there is only a small increase of the converted power between 30 and 40 V, for the same reason as in previous experiments. Figure 18 shows the total harvested power from noise vibrations at the input (figure 16). It has been calculated as the integral of the harvested PSD over the band [1 Hz–1 kHz] on the spectra shown in figure 17. As expected, the converted power increases as the square of the applied voltage, however, being very weak

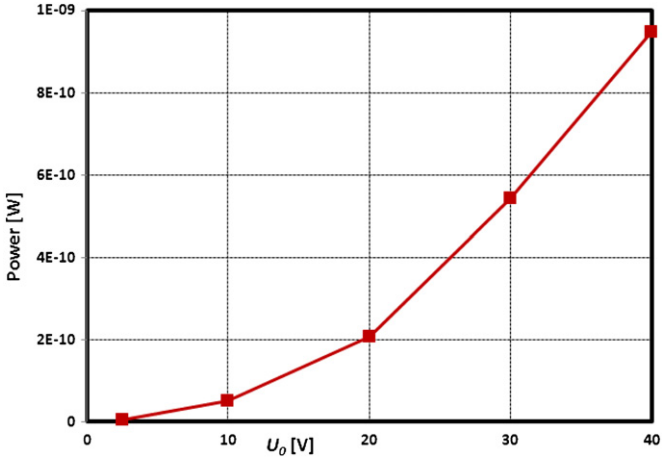


**Figure 18.** Total harvested power with the input noise in figure 16 over the band [1 Hz–1 kHz].

(∼1 nW at $U_0 = 40$ V). This can be explained by the fact that only a small part of the input power belongs to the frequency band in which the harvester is sensitive to the vibrations. In this experiment, the mass does not touch the stoppers, and because of the nonlinearity of the capacitive transducer, the converted power falls dramatically when the mobile mass amplitude decreases. The output power would be much higher if the same total acceleration was concentrated in the effective system bandwidth (i.e. 140–160 Hz) of the transducer.

## 5. Conclusion

We have presented a batch-fabricated MEMS e-VEH that has a very large half-power bandwidth of more than 30%. This is achieved by combining of two effects: electrostatic spring softening induced by the bias voltage and spring stiffening induced by the impact of the mobile mass with the rigid frame. The device has been tested with a basic conditioning circuit. This circuit has a complex behavior that has been studied in detail in order to predict the optimal resistance of the load. Our analysis is based on two methods. The first method presented in our previous works is based on the mechanical impedance, while the second method is based on the charge–voltage diagram. The mechanical impedance method can be used for any kind of VEHs with a large quality factor (>10), while the *QU* cycle method is valid only for e-VEHs.

A behavioral model of the system has been used for numerical simulations. There is a good correspondence between numerical simulations and the experiments at moderate external accelerations and bias voltages. However the model becomes approximate for high acceleration combined with high voltage. This can be explained by the fact that two nonlinear phenomena have not been taken into account in the model. For higher external accelerations, a more accurate model of the MEMS geometry is required together with a better model for nonlinear squeeze-film damping to match simulation results with the experiment. In addition, a discrepancy between the model and the experiment can be explained by the irregular dynamics of the mobile mass that

have not been included into the model and that modify the effective magnitude of the mobile mass motion.

The MEMS device has an area of about 1 $cm^2$. We measured the maximum converted power of 2.2 $\mu$W at atmospheric pressure for a 1 $g_{peak}$ harmonic vibration at 150 Hz and 30 V of bias voltage. This value is a lower than what is predicted by the theory (3.2 $\mu$W). The device displays a large frequency band of operation when excited with wideband stochastic noise.

At this stage, it is interesting to see what part of the power given by the fundamental limit equation (1) equal to 11 $\mu$W was actually converted into electricity. As was mentioned, the input mechanical power is split into two parts: power converted to electricity and dissipated power. The former is 2.2 $\mu$W in our system. The dominant dissipation mechanism is squeeze film damping. The dissipated power can be estimated considering viscous air damping with the measured $Q$-factor $Q = 4.5$ at large displacements, The damping factor can then be estimated as $\mu = m\omega_m/Q = 0.014$ Ns $m^{-1}$, and the dissipated power is $P = 0.5(\omega_m X_{\text{lim}})^2\mu = 8.0$ $\mu$W. We note that this estimation is approximate, since at large vibration amplitudes squeeze film damping cannot be considered as linear. The sum of the two powers gives 10.2 $\mu$W, which is not far from 11 $\mu$W given by the formula equation (1). In this way, the performance of the presented structure is close to its fundamental limit. In order to increase the converted power, air damping should be reduced (the structure should be placed in vacuum), and the parameters of the formula equation (1) should be increased, in particular, the mass of the resonator.

Soliman [42] and Halvorsen [25] have already shown how the impact of the mobile mass of a VEH can create a bi-stable system and increase the bandwidth of the harvested power toward frequencies higher than the natural resonance $f_0$ of the device. A similar behavior can also be obtained using nonlinear springs, for frequencies higher or lower than $f_0$ [16]. It is also well known that applying a voltage across the electrodes of an electrostatic transducer decreases its frequency of resonance. In this paper, we have studied the influence of the bias voltage on a silicon-based MEMS e-VEH with and without contact of the mobile mass with mechanical stoppers. We have observed that in contact mode, there is an optimum value of the bias voltage corresponding to a drastic increase of the bandwidth while keeping a maximum harvesting power for both harmonic and stochastic vibrations. From $U_0 = 20$ V, the mobile mass enters progressively into multistable mode that can be beneficial for harvesting power from stochastic noise. The highest power and bandwidth are obtained for $U_0 = 30$ V when harmonic vibrations are applied. For the input in form of low power colored noise, the optimal bias voltage is estimated 40 V.

## Acknowledgments

The authors gratefully acknowledge the support of the French National Research Agency through the contract ANR-08-SEGI-019, and the FP7 Marie Curie IEF funding scheme (NEHSTech, grant no 275437) at Université de Paris-Est, ESIEE Paris.

## References

[1] Basset P, Galayko D, Paracha A M, Marty F, Dudka A and Bourouina T 2009 A batch-fabricated and electret-free silicon electrostatic vibration energy harvester *J. Micromech. Microeng.* **19** 115025

[2] Hoffmann D, Folkmer B and Manoli Y 2009 Fabrication, characterization and modelling of electrostatic micro-generators *J. Micromech. Microeng.* **19** 094001

[3] Nguyen D S, Halvorsen E, Jensen G U and Vogl A 2010 Fabrication and characterization of a wideband MEMS energy harvester utilizing nonlinear springs *J. Micromech. Microeng.* **20** 125009

[4] Nada Y, Medhat M, Nagi M, Marty F, Saadany B and Bourouina T 2012 Mechanical displacement multiplier: 250 $\mu$m stable travel range MEMS actuator using frictionless simple compliant structures *MEMS'12: Proc. IEEE 25th Int. Conf. on Micro Electro Mechanical Systems* pp 1161–64

[5] Miki D, Honzumi M, Suzuki Y and Kasagi N 2012 Large-amplitude MEMS electret generator with non-linear spring *MEMS'10: Proc. IEEE 23rd Int. Conf. on Micro Electro Mechanical Systems* pp 176–79

[6] Boisseau S, Despesse G and Sylvestre A 2010 Optimization of an electret-based energy harvester *Smart Mater. Syst.* **19** 075015

[7] Ayala-Garcia I, Mitcheson P D, Yeatman E M, Zhu D, Tudor J and Beeby S P 2012 Magnetic tuning of a kinetic energy harvester using variable reluctance *Sensors Actuators* A **189** 266–75

[8] Galayko D, Basset P and Paracha A 2008 Optimization and AMS modeling for design of an electrostatic vibration energy harvester's conditioning circuit with an auto-adaptive process to the external vibration changes *MEMS/MOEMS'08: Symposium on Design, Test, Integration and Packaging of Micro- Electro-Mechanical Systems/Micro-Opto-Electro-Mechanical Systems* pp 302–6

[9] Eichhorn C, Tchagsim R, Wilhelm N and Woias P 2011 A smart and self-sufficient frequency tunable vibration energy harvester *J. Micromech. Microeng.* **21** 104003

[10] Koyama D and Nakamura K 2009 Array configurations for higher power generation in piezoelectric energy harvesting *IEEE Ultrasonics Symposium (September 2009)* pp 1973–6

[11] Xue H, Hu Y and Wang Q M 2008 Broadband piezoelectric energy harvesting devices using multiple bimorphs with different operating frequencies *IEEE Trans. Ultrason. Ferroelectr. Freq. Control* **55** 2104–8

[12] Shan X B, Yuan J B, Xie T and Chen W S 2010 Design and experiment of multiple piezoelectric bimorphs for scavenging vibration energy *Int. J. Appl. Electromagn. Mech.* **34** 265–75

[13] Yang B, Lee C, Xiang W, Xie J, He J H, Kotlanka R K, Low S P and Feng H 2009 Electromagnetic energy harvesting from vibrations of multiple frequencies *J. Micromech. Microeng.* **19** 035001

[14] Cottone F, Vocca H and Gammaitoni L 2009 Nonlinear energy harvesting *Phys. Rev. Lett.* **102** 080601

[15] Marzencki M, Defosseux M and Basrour S 2009 MEMS vibration energy harvesting devices with passive resonance adaptation capability *J. Microelectromech.* **18** 1444–53

[16] Amri M, Basset P, Cottone F, Galayko D, Najar F and Bourouina T 2011 Novel nonlinear spring design for wideband vibration energy harvesters *PowerMEMS'12: Proc. Power MEMS* pp 189–92

[17] Miki D, Honzumi M, Suzuki Y and Kasagi N 2010 Large amplitude MEMS electret generator with nonlinear spring *MEMS'10: IEEE 23rd Int. Conf. on Micro Electro Mechanical Systems* pp 176–9
[18] Burrow S and Clare L 2007 A resonant generator with non-linear compliance for energy harvesting in high vibrational environments *IEMDC'07: IEEE Int. Electric Machines and Drives Conference* pp 715–20
[19] Erturk A and Inman D J 2010 Broadband piezoelectric power generation on high-energy orbits of the bistable Duffing oscillator with electromechanical coupling *J. Sound Vib.* **330** 2339–53
[20] Stanton S C, McGehee C C and Mann B P 2010 Nonlinear dynamics for broadband energy harvesting: Investigation of a bistable piezoelectric inertial generator *Physica* D **239** 640–53
[21] Cottone F, Gammaitoni L, Vocca H, Ferrari M and Ferrari V 2012 Piezoelectric buckled beams for random vibration energy harvesting *Smart Mater. Struct.* **21** 035021
[22] Cottone F, Basset P, Vocca H and Gammaitoni L 2012 Electromagnetic buckled beam oscillator for enhanced vibration energy harvesting *IEEE Conf. on Green Computing and Comms. (November 2012)* pp 624–27
[23] Liu W Q, Badel A, Formosa F, Wu Y P and Agbossou A 2013 Novel piezoelectric bistable oscillator architecture for wideband vibration energy harvesting *Smart Mater. Struct.* **22** 035013
[24] Cottone F, Basset P, Guillemet R, Galayko D, Marty F and Bourouina T 2013 Non-linear MEMS electrostatic kinetic energy harvester with a tunable multistable potential for stochastic vibrations *Transducers'13: Proc. 17th Int. Conf. on Solid-State Sensors, Actuators and Microsystems (Barcelona, Spain)* pp 1336–9
[25] Phu Le C and Halvorsen E 2012 MEMS electrostatic energy harvesters with end-stop effects *J. Micromech. Microeng.* **22** 074013
[26] Paracha A M, Basset P, Lim P C L, Marty F and Bourouina T 2006 A bulk silicon-based electrostatic vibration-to-electricity energy converter using in-plane-overlap-plate (IPOP) mechanism *PowerMEMS'06: Proc. 6th Int. Workshop on Micro and Nanotechnology for Power Generation and Energy Conversion Applications (Berkeley, CA)* pp 169–72
[27] Roundy S J 2003 Energy scavenging for wireless sensor nodes *PhD Thesis* University of California-Berkeley
[28] Guillemet R, Basset P, Galayko D, Marty F and Bourouina T 2012 Efficient in-plane gap-closing MEMS electrostatic vibration energy harvester *PowerMEMS'12: Proc. 12th Int. Workshop on Micro and Nanotechnology for Power Generation and Energy Conversion Applications (Atlanta, GA)*
[29] Guillemet R *et al* 2013 Wideband MEMS electrostatic vibration energy harvesters based on gap-closing interdigited combs with a trapezoidal section *IEEE 26th Int. Conf. on MEMS (Taipei, 2013)*
[30] Mitcheson P D, Green T C, Yeatman E M and Holmes A S 2004 Architectures for vibration-driven micropower generators *J. Microelectromech. Syst.* **13** 429–40
[31] Blokhina E, Galayko D, Harte P, Basset P and Feely O 2012 Limit on converted power in resonant electrostatic vibration energy harvesters *Appl. Phys. Lett.* **101** 173904
[32] Mitcheson P D, Sterken T, He C, Kiziroglou M, Yeatman E M and Puers R 2008 Electrostatic microgenerators *Meas. Control* **41** 114
[33] Dudka A, Galayko D and Basset P 2013 IC design of an adaptive electrostatic vibration energy harvester: focus on clock generator *DTIP: Proc. 15th Symp. on Design, Test, Integration and Packaging Conference, (Barcelona, Spain)*
[34] Meninger S, Mur-Miranda J O, Amirtharajah R, Chandrakasan A P and Lang J H 2001 Vibration-to-electric energy conversion *IEEE Trans. Very Large Scale Integr. (VLSI) Syst.* **9** 64–76
[35] Yen B C and Lang J H 2006 A variable capacitance vibration to electric energy harvester *IEEE Trans. Circuits Syst.* **53** 288–95
[36] Galayko D, Basset P and Paracha A 2008 Optimization and AMS modeling for design of an electrostatic vibration energy harverster's conditioning circuit with an auto-adaptative process to the external vibration changes *DTIP'08: Proc. 10th Symp. on Design, Test, Integration and Packaging Conference (Nice, France)*
[37] Galayko D and Basset P 2011 A general analytical tool for the design of vibration energy harvesters (VEHs) based on the mechanical impedance concept *IEEE Trans. Circuits Syst.*. **58** 299–311
[38] Landau L D and Lifshitz E M 1976 Mechanics *Course of Theoretical Physics* 3rd edn vol 1 (Amsterdam: Elsevier)
[39] Nayfeh A H and Mook D T 1995 *Nonlinear Oscillations* (New York: Wiley)
[40] Senturia S 2001 *Microsystem Design* (Dordrecht: Kluwer)
[41] Steeneken P G, Rijks T G, Van Beek J T M, Ulenaers M J E, De Coster J and Puers R 2005 Dynamics and squeeze film gas damping of a capacitive RF MEMS switch *J. Micromech. Microeng.* **15** 176
[42] Soliman M, Abdel-Rahman E M, El-Saadany E F and Mansour R R 2008 A wideband vibration-based energy harvester *J. Micromech. Microeng.* **18** 115021
[43] Cottone F, Basset P, Guillemet R, Galayko D, Marty F and Bourouina T 2013 Non-linear MEMS electrostatic kinetic energy harvester with a tunable multistable potential for stochastic vibrations *Transducers'13: Proc. 17th Int. Conf. on Solid-State Sensors, Actuators and Microsystems (Barcelona, Spain)*
[44] Blokhina E, Galayko D, Basset P and Feely O 2013 Steady-state oscillations in electrostatic vibration energy harvesters *IEEE Trans. Circuits Syst.* **60** 875–84